 doi:10.20944/preprints201904.0328.v1

Peer-reviewed version available at *Fluids* **2019**, *4*, 101; doi:10.3390/fluids4020101

Article

On moderate-Rayleigh-number convection in an inclined porous layer

Baole Wen [1,2]* and Gregory P. Chini [3,4]*

[1] Institute of Computational Engineering and Sciences, The University of Texas at Austin, Austin, Texas 78712, USA
[2] Department of Geological Sciences, University of Texas at Austin, Austin, TX 78712, USA; wenbaole@gmail.com
[3] Program in Integrated Applied Mathematics, University of New Hampshire, Durham, NH 03824, USA
[4] Department of Mechanical Engineering, University of New Hampshire, Durham, NH 03824, USA; greg.chini@unh.edu
* Correspondence: wenbaole@gmail.com (B.W.); greg.chini@unh.edu (G.P.C.)

Version April 29, 2019 submitted to Preprints

Abstract: We investigate the flow structure and dynamics of moderate-Rayleigh-number (Ra) thermal convection in a two-dimensional inclined porous layer. Direct numerical simulations (DNS) confirm the emergence of $O(1)$ aspect-ratio large-scale convective rolls, with one 'natural' roll rotating in the counterclockwise direction and one 'antinatural' roll rotating in the clockwise direction. As the inclination angle ϕ is increased, the background mean shear flow intensifies the natural-roll motion, while suppressing the antinatural-roll motion. Moreover, our DNS reveal—for the first time in single-species porous medium convection—the existence of *spatially-localized* convective states at large ϕ, which we suggest are enabled by subcritical instability of the base state at sufficiently large inclination angles. To better understand the physics of inclined porous medium convection at different ϕ, we numerically compute steady convective solutions using Newton iteration and then perform secondary stability analysis of these nonlinear states using Floquet theory. Our analysis indicates that the inclination of the porous layer stabilizes the boundary layers of the natural roll, but intensifies the boundary-layer instability of the antinatural roll. These results facilitate physical understanding of the large-scale cellular flows observed in the DNS at different values of ϕ.

Keywords: convection; porous media; secondary stability; Floquet theory; localized states

---

1. Introduction

Buoyancy-driven convection in fluid-saturated porous media exhibits rich instability characteristics and nonlinear dynamics as the Rayleigh number Ra, the ratio of driving to damping forces, increases [1–7]. This system has been extensively studied owing to applications in geothermal energy extraction, geological carbon sequestration, and the the design of compact heat exchangers [8–11]. In a homogenous and isotropic *horizontal* porous layer uniformly heated from below, the basic conduction state becomes linearly unstable above a critical Rayleigh number $Ra_c = 4\pi^2$ [1,2], giving rise to steady $O(1)$ aspect-ratio large-scale convective rolls through a stationary bifurcation. As Ra is increased further, a secondary instability occurs within the upper and lower thermal boundary layers via a supercritical Hopf bifurcation, generating small-scale plumes that are periodically or quasi-periodically advected around the cells for $400 \lesssim Ra \lesssim 1300$ [3,12–16]. For $Ra > 1300$, the large-scale cellular flow is broken down and the system transitions to the 'turbulent', narrowly spaced columnar-flow, high-Ra regime [4–6].

In deep geological formations the layer may not be strictly horizontal; for example, in carbon sequestration the saline aquifers are generally inclined at an angle to the horizontal [17–20]. The inclination of the layer introduces an additional control parameter, i.e., the tilt angle, which significantly affects the instability and bifurcation of the base flow. In a sloping three-dimensional (3D) porous

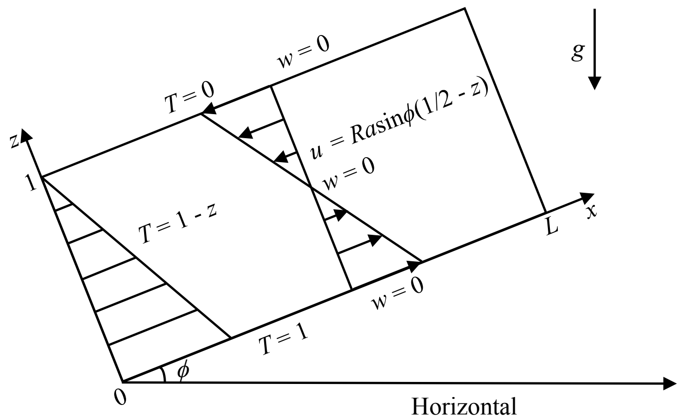

Figure 1. Dimensionless geometry and background/basic state for 2D convection in an inclined Rayleigh–Darcy domain. x and z are the wall-parallel and wall-normal coordinates, respectively, and g is the (dimensional) acceleration of gravity. For $\phi > 0^\circ$, the basic-state temperature field (realized in the absence of convection) varies only in z, as in the horizontal case ($\phi = 0^\circ$). The basic-state velocity field is nonzero, however, with the background x-directed shear flow strengthening as the inclination angle ϕ is increased.

layer with an inclination angle ϕ above the horizontal, four types of flows exist near the onset of convection: the basic single-cell shear flow with an upward current near the lower heated wall and a downward current near the upper cooled wall; polyhedral cells with wall-normal axes; longitudinal helicoidal cells resulting from the longitudinal rolls (with wall-parallel axes) superposed on the basic flow; and two-dimensional (2D) transverse rolls [21–34]. Note that in an infinitely extended layer, the unicellular base state becomes independent of the wall-parallel (x) coordinate and reduces to a laminar unidirectional shear flow, as schematically depicted in figure 1. The early experiments by Bories and collaborators [21–23] indicated that the basic unicellular flow is stable for $Ra \cos\phi \leq 4\pi^2$; when $Ra \cos\phi$ is slightly greater than $4\pi^2$, however, convection appears in the form of polyhedral cells for small inclination angles ($\phi \lesssim 15^\circ$) and longitudinal helicoidal rolls for larger ϕ. Besides these three flow configurations, 2D transverse rolls are also observed at small Ra and ϕ, e.g., in the experiments by Caltagirone *et al.* [24], Kaneko [25], and Kaneko *et al.* [26], and in the numerical simulations by Caltagirone and Bories [27].

In order to investigate the conditions for transitions between these different flow regimes, a series of subsequent studies were carried out. Using linear stability analysis, Caltagirone and Bories [27] demonstrated that in an infinitely extended porous layer, the basic-state shear flow is stable for $Ra \cos\phi \leq 4\pi^2$. These authors also obtained a transition criterion from the polyhedric cells or transverse rolls to the helicoidal cells, with their analysis yielding a transition angle $\phi_t \simeq 31.8^\circ$ between these flow patterns. More recently, a full numerical investigation of the marginal stability of the background mean flow was performed by Rees and Bassom [28] in a 2D inclined porous layer. Since all fields are presumed to be independent of the transverse (y) direction, polyhedric cells and helicoidal rolls cannot be realized in the 2D layer. Consequently, the basic unicellular flow can be linearly stable at smaller ϕ. Moreover, as shown in Reference [28], at *large Ra* 2D linear instability can only arise when $\phi \leq 31.3^\circ$. Additional linear stability analyses have been performed with the aim of understanding the effects of material anisotropy and variations in boundary conditions [29–34]. Crucially, recent analysis by Wen and Chini [35] indicates that the basic state is not *energy* stable for $\phi \leq 90^\circ$ and $Ra > 91.6$, so this base state may become unstable to sufficiently large-amplitude disturbances for $\phi > 31.3^\circ$.

Instead of focusing on the onset of convection, in this work we study numerically how layer inclination affects the flow structure and dynamics of *finite-amplitude* convection at moderate values of the Rayleigh number ($Ra < 1000$). Although some numerical simulations have been performed in inclined cavities to investigate the steady convective flow at small Ra [36–38], the side walls may

Preprints (www.preprints.org) | NOT PEER-REVIEWED | Posted: 30 April 2019 doi:10.20944/preprints201904.0328.v1

Peer-reviewed version available at Fluids 2019, 4, 101; doi:10.3390/fluids4020101

significantly impact the flow structure and transport properties if the aspect ratio of the domain is not sufficiently large (e.g., in a sloping *square* cavity). Here, we conduct direct numerical simulations (DNS) in inclined 2D Rayleigh–Darcy domains with large aspect ratios and periodic boundary conditions in the wall-parallel (x) direction. Moreover, to investigate the physical mechanisms manifested in the DNS at different Ra and ϕ, we compute (generally unstable) *steady* convective solutions using Newton iteration and then perform secondary stability analysis of these nonlinear states numerically using Floquet theory. Our results confirm that investigation of the steady solutions does, indeed, shed light on the development of moderate-Ra large-scale cellular flows at different inclination angles.

The remainder of this paper is organized as follows. In the following section, we formulate the standard mathematical model of inclined porous medium convection. In § 3, we perform DNS in the moderate-Ra regime at different inclination angles, and investigate the structure and stability of steady nonlinear convective states numerically. Finally, our conclusions are given in § 4.

2. Governing Equations

Consider a 2D, homogenous and isotropic, fluid-saturated porous layer inclined at an angle ϕ above the horizontal (figure 1). The domain is heated from below and has aspect ratio L. We assume the motion of the incompressible fluid satisfies the Boussinesq approximation and Darcy's law. Then, the flow and heat transport processes of the system are governed by the following non-dimensional equations [10]:

$$\nabla \cdot \mathbf{u} = 0, \tag{1}$$
$$\mathbf{u} + \nabla p = RaT(\sin\phi \mathbf{e}_x + \cos\phi \mathbf{e}_z), \tag{2}$$
$$\partial_t T + \mathbf{u} \cdot \nabla T = \nabla^2 T, \tag{3}$$

where $\mathbf{u}(\mathbf{x}, t) = (u, w)$, $T(\mathbf{x}, t)$ and $p(\mathbf{x}, t)$ are the dimensionless velocity, temperature, and pressure, respectively; $\mathbf{e}_x$ and $\mathbf{e}_z$ are unit vectors in the wall-parallel (x) and wall-normal (z) directions; and ∇^2 is the 2D Laplacian operator. The system of equations is solved subject to the boundary conditions

$$T(x, 0, t) = 1, \quad T(x, 1, t) = 0, \quad w(x, 0, t) = 0, \quad w(x, 1, t) = 0. \tag{4}$$

All fields are required to be L-periodic in x. For the 2D system, the fluid velocity can be described by using a stream function ψ, so that $(u, w) = (\partial_z \psi, -\partial_x \psi)$. Then equations (2) and (3) can be re-expressed as

$$\nabla^2 \psi = Ra(\partial_z \theta \sin\phi - \sin\phi - \partial_x \theta \cos\phi), \tag{5}$$
$$\partial_t \theta + \partial_z \psi \partial_x \theta - \partial_x \psi \partial_z \theta = -\partial_x \psi + \nabla^2 \theta, \tag{6}$$

where $\theta(\mathbf{x}, t) = T(\mathbf{x}, t) - (1 - z)$, and θ and ψ satisfy L-periodic boundary conditions in x and homogeneous Dirichlet boundary conditions in z.

Three dimensionless parameters control the dynamics of this system: the inclination angle ϕ; the domain aspect ratio L; and the normalized temperature drop across the layer, namely, the Rayleigh-Darcy number

$$Ra = \frac{HKg\alpha\Delta T}{\kappa\nu}, \tag{7}$$

where H is the layer thickness, K is the medium permeability, g is the gravitational acceleration, α is the thermal expansion coefficient, ΔT is the temperature difference across the layer, κ is the thermal diffusivity, and ν is the kinematic viscosity. In an infinitely extended layer, the inclination of the domain will induce a background (mean) shear-flow solution which strengthens as ϕ is increased: $T = 1 - z$, $\mathbf{u} = Ra\sin\phi(\frac{1}{2} - z)\mathbf{e}_x$ and $p = \frac{1}{2}Ra\sin\phi x + Ra\cos\phi(z - \frac{1}{2}z^2)$, as shown schematically in

Preprints (www.preprints.org) | NOT PEER-REVIEWED | Posted: 30 April 2019 doi:10.20944/preprints201904.0328.v1

Peer-reviewed version available at Fluids 2019, 4, 101; doi:10.3390/fluids4020101

figure 1. In the next section, we demonstrate that this background shear flow dramatically impacts the flow structure as ϕ is increased.

3. Dynamics at moderate *Ra*

3.1. DNS results

In this section, DNS are performed to investigate the dynamics of convection at moderate *Ra* in an inclined porous layer. We solve equations (5) and (6) numerically using a Fourier–Chebyshev-tau pseudospectral solver developed in References [35,39–41]. The system is discretized spatially using Fourier series in x and Chebyshev series in z [42], and temporally using a third-order-accurate semi-implicit Runge–Kutta scheme for the first three time steps [43] and a four-step fourth-order-accurate semi-implicit Adams–Bashforth/Backward-Differentiation scheme for all subsequent time steps [44].

At small *Ra* (just above the onset of convection), the flow exhibits steady stable $O(1)$ aspect-ratio large-scale convective rolls when the layer is inclined. As shown in figure 2, for $Ra = 100$ and $L = 2$ there exist two steady cells corresponding to counter-rotating convective rolls: the counterclockwise circulation with positive ψ and the clockwise circulation with negative ψ, hereafter referred to as 'natural' and 'antinatural' convective rolls, respectively. Either of these two types of steady circulation may exist in isolation in the small-aspect-ratio sloping porous *cavity* due to the effect of thermally-insulating lateral walls [37,38]; however, in a periodic domain, these two rolls always coexist. Moreover, for the horizontal case ($\phi = 0°$), the steady flow exhibits centro-reflection symmetry (figure 2a). Reflection symmetry in x is broken by the layer inclination ($0° < \phi < 90°$), although centrosymmetry is retained (figure 2b, c). Our DNS results indicate that the inclination of the layer modifies the boundary layer thickness of the velocity field for the natural and antinatural rolls: the former becomes thinner while the latter becomes thicker. Furthermore, the extremum ψ value of the natural roll becomes larger as ϕ is increased (see the colorbar limits in figure 2), in contrast to that of the antinatural roll, implying that compared with antinatural convective motion, the natural convective motion becomes more vigorous when the layer is inclined. This result accords with the physical intuition that, for $0° < \phi < 90°$, the base shear flow enhances (suppresses) fluid motions with the same (opposite) sense of rotation.

As for horizontal convection, the steady rolls computed at different ϕ strengthen but remain stable as *Ra* is increased up to 200. As shown in figure 3, however, at $Ra = 300$ the antinatural roll becomes unstable first for $\phi \gtrsim 10°$ (while the natural roll remains stable) and small-scale proto-plumes are generated from the upper and lower thermal boundary layers and advected around the cell by the background roll (figure 3c). Moreover, this boundary layer instability becomes much stronger as the inclination angle is increased so that the two-cell (one natural and one antinatural) unsteady convective rolls are split into the four-cell stable steady convective rolls at $\phi \approx 25°$, as shown in figure 3(d).

For $Ra \gtrsim 400$, the steady convective rolls become unstable even at small ϕ, and the resulting flow exhibits a series of transitions between periodic and quasi-periodic roll motions (figure 4), as observed in the horizontal case. A primary difference between inclined and horizontal porous medium convection is that the inclination of the layer alters the symmetry of the flow by intensifying the near-wall instability of the antinatural (associated with a thickening of the velocity boundary layer) while stabilizing the natural roll (associated with a thinning of the velocity boundary layer). As ϕ is increased, the boundary-layer instability of the antinatural roll becomes more vigorous so that the plumes generated from the thermal boundary layers split the original two-cell convection into multiple-cell convection, as shown in figure 4. It is worth noting that as *Ra* is increased, the value of ϕ at which the flow transitions from two-cell convection to four-cell convection decreases (table 1), e.g., for $Ra = 300$, 500 and 998, the approximate transition angle is decreased from 25° to 15° and finally to 5°.

Preprints (www.preprints.org) | NOT PEER-REVIEWED | Posted: 30 April 2019 doi:10.20944/preprints201904.0328.v1

Peer-reviewed version available at *Fluids* **2019**, *4*, 101; doi:10.3390/fluids4020101

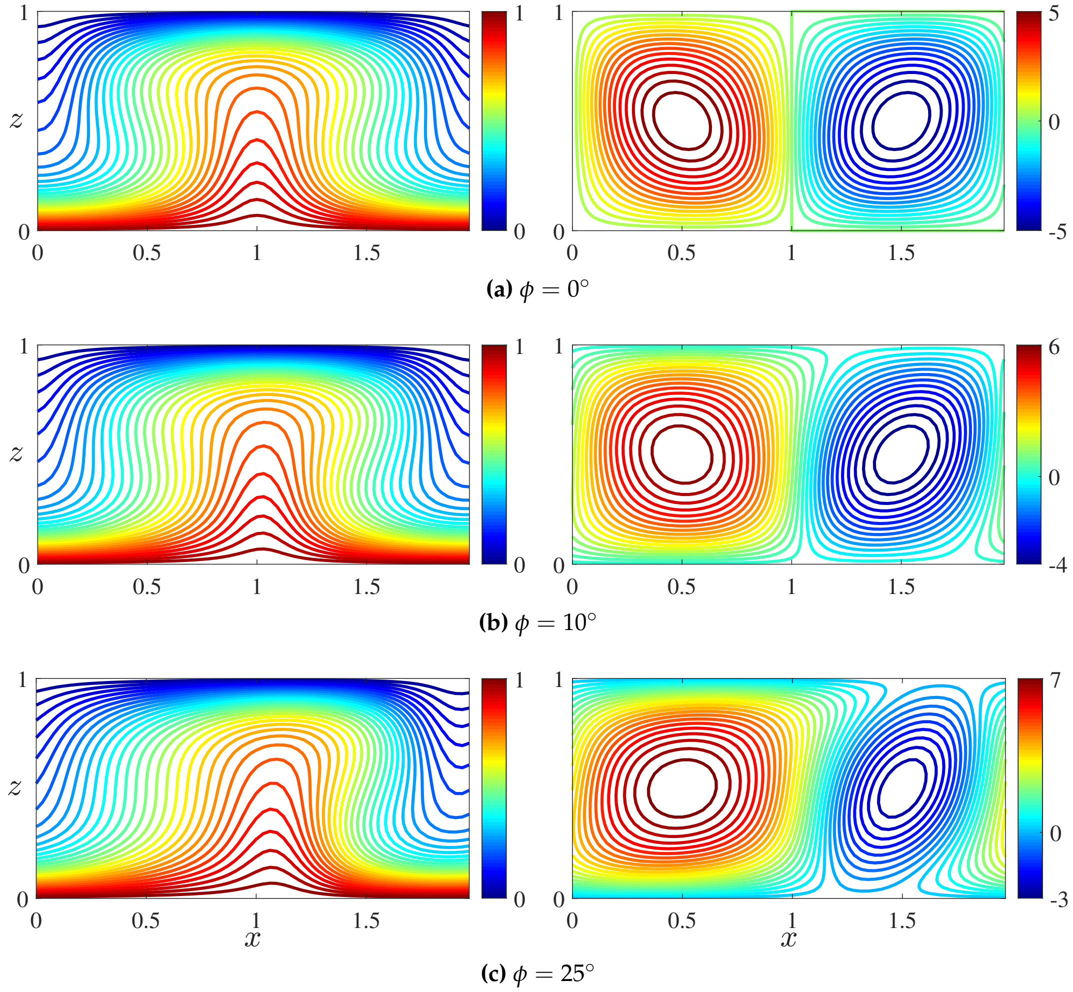

Figure 2. Snapshots of isotherms (left) and corresponding streamlines (right) from DNS at $Ra = 100$ and $L = 2$. The streamlines of the natural (positive ψ) and antinatural (negative ψ) rolls are shown in red and blue, respectively. The flow takes the form of stable and steady convective rolls at different ϕ. As ϕ is increased, the natural roll becomes more vigorous (see the colorbar limits) and more tightly attached to the walls, while the antinatural roll is suppressed and becomes detached from the walls.

Table 1. Approximate angle ϕ at which the flow transitions from two-cell convection to four-cell convection in DNS at moderate Ra.

$\boldsymbol{Ra}$	300	500	792	998
$\boldsymbol{\phi}$	25°	15°	10°	5°

The 2D numerical simulations performed by Caltagirone and Bories [27] and Moya *et al.* [37] did not exhibit convective flows at large ϕ in wide domains (e.g., $L = 10$), in apparent agreement with the prediction that the basic state is *linearly* stable for $\phi > \phi_t$ with $\phi_t \approx 31.3°$ [28]. Nevertheless, the basic state may become unstable when disturbance amplitudes are sufficiently large since, as shown by Wen and Chini [35], the base state is not energy stable for $\phi \leq 90°$ at $Ra > 91.6$. Figure 5 shows snapshots of isotherms from DNS at $\phi = 35°$ and $L = 10$ for different Rayleigh numbers ranging from 100 to 500. Interestingly, not only do convective flows arise but, given different initial conditions, these convective flows can adopt distinct forms. For instance, at $Ra = 100$, the flow can exhibit stable *localized* convective structures with various numbers of roll pairs (figure 5a, b) or large-scale cellular flows (figure 5c); however, it can also exist as five replicas of a stable two-cell convective state obtained from $L = 2$ (figure 5d). We note that spatially-localized states previously have been

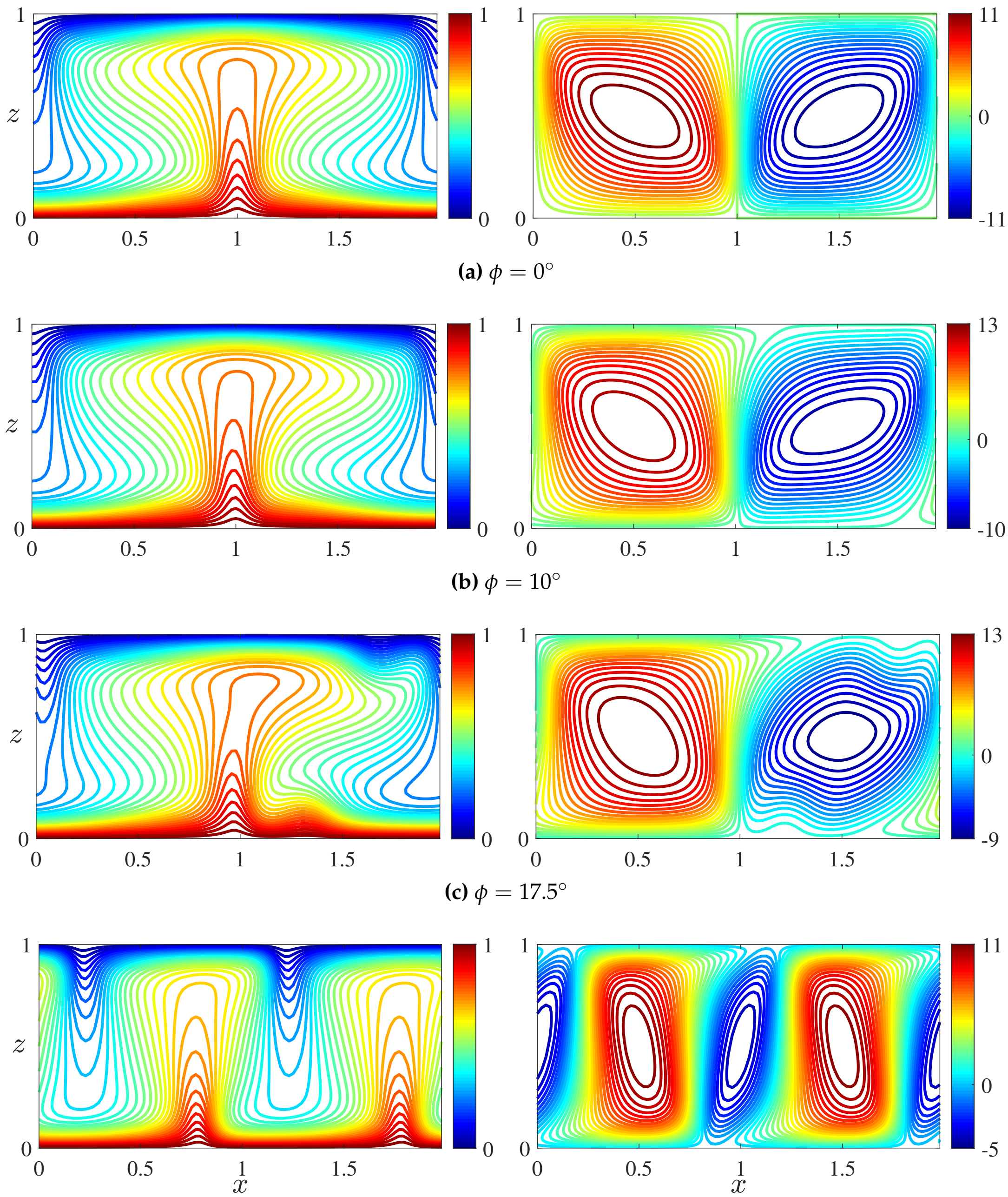

(a) $\phi = 0°$

(b) $\phi = 10°$

(c) $\phi = 17.5°$

(d) $\phi = 25°$

Figure 3. Snapshots of isotherms (left) and corresponding streamlines (right) from DNS at $Ra = 300$ and $L = 2$. In this case, the flows in (a) and (d) are steady; in (b) and (c), the upper and lower boundary layers of the antinatural rolls (negative ψ) become unstable. At $\phi \approx 25°$, the small proto-plumes generated from the boundary-layer instabilities of the antinatural rolls split the unsteady two-cell convection (one natural roll and one antinatural roll) into a steady four-cell convective state, thereby reducing the aspect ratio of each roll.

observed in double-diffusive convection in porous media [45,46], but here our DNS reveal—for the first time in single-species porous medium convection—the existence of these localized convective states at large ϕ. Moreover, our DNS results also indicate that the (large-scale) localized roll pattern still appears instantaneously at higher Ra when the flow becomes unsteady (figure 5e, f). Although the flow structure for $\phi > \phi_t$ at small and moderate Ra will not be discussed in further detail in this study, we comment that this spatially-localized convective state appears to arise through a subcritical

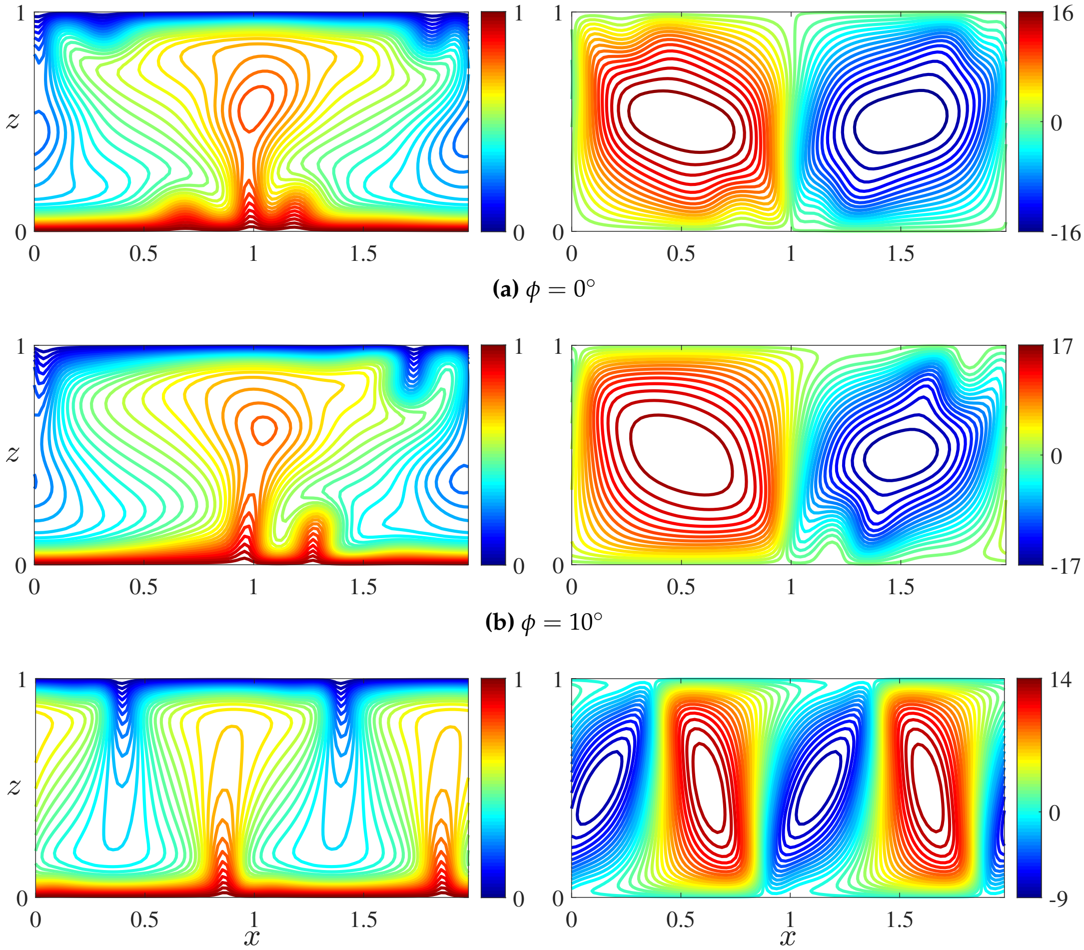

(a) $\phi = 0°$

(b) $\phi = 10°$

(c) $\phi = 15°$

Figure 4. Snapshots of isotherms (left) and corresponding streamlines (right) from DNS at $Ra = 500$ and $L = 2$. For $\phi < 15°$, the convection appears in the form of unsteady rolls (a, b). However, as ϕ is increased, the boundary-layer instability of the antinatural roll (negative ψ) becomes stronger and splits the unsteady two-cell convective state into the steady four-cell convection pattern.

bifurcation of the basic unicellular state enabled by the gap in parameter values for linear and nonlinear stability [35].

In summary, our DNS show that the instantaneous flow at moderate Ra self-organizes into $O(1)$ aspect-ratio large-scale cellular flows, suggesting that the basic physics of inclined porous medium convection can be understood by studying the underlying *exact coherent states*, e.g., steady convective solutions, that support observed convective patterns. Accordingly, in the following sections, we compute steady convective solutions and then assess the stability of these nonlinear states.

3.2. Steady convective states

We numerically compute the steady solutions of equations (5)–(6) using the Newton–GMRES (generalized minimal residuals) algorithm. Following Wen *et al.* [6] and Wen and Chini [35], we write the linear differential equations for the corrections as

$$\begin{bmatrix} \nabla^2 & Ra(\cos\phi\partial_x - \sin\phi\partial_z) \\ -\partial_x + \theta_z^i\partial_x - \theta_x^i\partial_z & \nabla^2 - \psi_z^i\partial_x + \psi_x^i\partial_z \end{bmatrix} \begin{bmatrix} \triangle^\psi \\ \triangle^\theta \end{bmatrix} = \begin{bmatrix} -F_{res}^\psi \\ -F_{res}^\theta \end{bmatrix}^i, \tag{8}$$

Preprints (www.preprints.org) | NOT PEER-REVIEWED | Posted: 30 April 2019 doi:10.20944/preprints201904.0328.v1

Peer-reviewed version available at *Fluids* **2019**, *4*, 101; doi:10.3390/fluids4020101

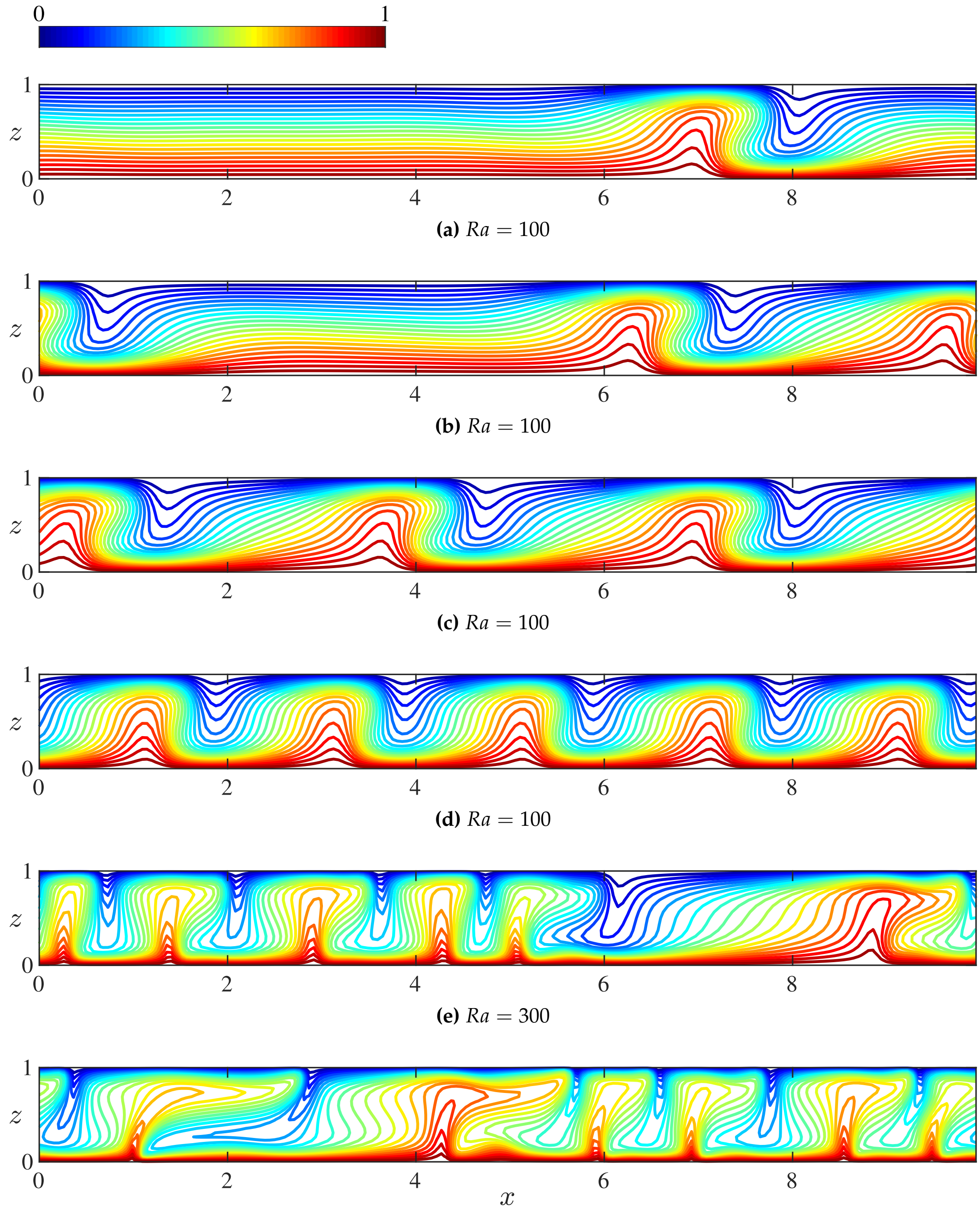

(a) $Ra = 100$

(b) $Ra = 100$

(c) $Ra = 100$

(d) $Ra = 100$

(e) $Ra = 300$

(f) $Ra = 500$

Figure 5. Snapshots of isotherms from DNS at $\phi = 35°$ and $L = 10$. Sub-plots (a-d) show steady convective states obtained using different initial conditions, while (e) and (f) show snapshots of time-dependent states. Although the basic-state shear flow is linearly stable for $\phi > \phi_t \approx 31.3°$ in 2D, convection nevertheless may be realized by initializing with sufficiently large-amplitude disturbances; i.e., *sub-critical* instabilities are possible in this parameter regime. The *spatially-localized* convective states evident in (a, b), observed here for the first time in single-species porous medium convection, are one manifestation of this sub-critical instability.

173 with the correction terms

$$\triangle^{\psi} = \psi^{i+1} - \psi^{i}, \quad \triangle^{\theta} = \theta^{i+1} - \theta^{i}, \tag{9}$$

Preprints (www.preprints.org) | NOT PEER-REVIEWED | Posted: 30 April 2019 doi:10.20944/preprints201904.0328.v1

Peer-reviewed version available at Fluids 2019, 4, 101; doi:10.3390/fluids4020101

174 and the residuals of the steady governing equations

$$F^{\psi}_{res} = \nabla^2\psi - Ra(\partial_z\theta\sin\phi - \sin\phi - \partial_x\theta\cos\phi), \tag{10}$$
$$F^{\theta}_{res} = \nabla^2\theta - (\partial_z\psi\partial_x\theta - \partial_x\psi\partial_z\theta + \partial_x\psi), \tag{11}$$

175 where the superscript 'i' denotes the ith Newton iterate. Then, (8) is solved using a Krylov-subspace
176 (GMRES) iterative method under the centrosymmetry constraint for θ. For each i, we stop the GMRES
177 iteration once the L2-norm of the residual of (8) is less than 10^{-4}, and finally stop the Newton iteration
178 when the L2-norm of $(F^{\psi}_{res}, F^{\theta}_{res})$ is less than 10^{-8}. For each Ra, the results from smaller ϕ are utilized as
179 the initial conditions for simulations at larger ϕ.
180 As noted above, steady convective states in an inclined porous layer are stable at small Ra (e.g.,
181 $Ra \le 200$). However, as the Rayleigh number is increased, the boundary layers near the upper and
182 lower walls become unstable and small-scale features are generated and advected around the cell by
183 the large-scale roll (figure 3c). In this section, the structure of the *unstable* steady convective states
184 is investigated at $Ra = 500$ and $L = 2$ for different inclination angles. As shown in figure 6, the
185 increasing inclination of the layer enhances the motion of the background flow, thereby intensifying
186 the natural-roll motion and suppressing the antinatural-roll motion. Consequently, as ϕ is increased,
187 the natural rolls become more vigorous and more tightly attached to the upper and lower walls; in
188 contrast, the antinatural rolls become much weaker and detach from the walls (figures 6 and 7).

189 *3.3. Secondary stability analysis*

190 In this section, a spatial Floquet analysis is performed to investigate the linear stability of the
191 fully nonlinear steady convective states in an inclined porous layer. We decompose each field into the
192 steady *nonlinear* (fully 2D) base flow (denoted with a subscript 's') plus a time-varying small-amplitude
193 perturbation (denoted with a tilde),

$$\psi(\mathbf{x},t) = \psi_s(\mathbf{x}) + \tilde{\psi}(\mathbf{x},t), \tag{12}$$
$$\theta(\mathbf{x},t) = \theta_s(\mathbf{x}) + \tilde{\theta}(\mathbf{x},t). \tag{13}$$

194 Then, the evolution of the disturbances $\tilde{\psi}$ and $\tilde{\theta}$ are governed by following linearized equations

$$\nabla^2\tilde{\psi} = Ra(\sin\phi\partial_z - \cos\phi\partial_x)\tilde{\theta}, \tag{14}$$
$$\partial_t\tilde{\theta} = \nabla^2\tilde{\theta} - \partial_x\theta_s\partial_z\tilde{\psi} + \partial_z\theta_s\partial_x\tilde{\psi} + \partial_x\psi_s\partial_z\tilde{\theta} - \partial_z\psi_s\partial_x\tilde{\theta} - \partial_x\tilde{\psi}. \tag{15}$$

195 According to Floquet theory, the solutions for the perturbations in (14) and (15) can be expressed as

$$\begin{bmatrix} \tilde{\theta} \\ \tilde{\psi} \end{bmatrix} = e^{i\beta k_s x}\left\{\sum_{n=-\infty}^{\infty}\begin{bmatrix} \hat{\tilde{\theta}}_n(z) \\ \hat{\tilde{\psi}}_n(z) \end{bmatrix} e^{ink_s x}\right\} e^{\lambda t} + c.c., \tag{16}$$

196 where λ is the temporal growth rate, k_s is the fundamental wavenumber of the spatially-periodic steady
197 solution, n is the wall-parallel Fourier mode number, β is the real Floquet parameter ($0 \le \beta \le 0.5$),
198 which provides the freedom to modify the fundamental horizontal wavenumber of the perturbation,
199 and $c.c.$ denotes complex conjugate. Substituting the ansatz (16) into equations (14)–(15) yields

$$-Ra\left[\sin\phi\partial_z - i(n+\beta)k_s\cos\phi\right]\hat{\tilde{\theta}}_n + \left[\partial_z^2 - (n+\beta)^2k_s^2\right]\hat{\tilde{\psi}}_n = 0, \tag{17}$$
$$\left[\partial_z^2 - (n+\beta)^2k_s^2 + \tilde{h}_n\right]\hat{\tilde{\theta}}_n + \left[-i(n+\beta)k_s + \tilde{g}_n\right]\hat{\tilde{\psi}}_n = \lambda\hat{\tilde{\theta}}_n \tag{18}$$

200 for each n, where $\tilde{h}_n$ and $\tilde{g}_n$ can be determined by calculating the convolution of the
201 non-constant-coefficient terms in (15). Finally, the eigenvalue problem (17)–(18) is discretized using a

Preprints (www.preprints.org) | NOT PEER-REVIEWED | Posted: 30 April 2019 doi:10.20944/preprints201904.0328.v1

Peer-reviewed version available at *Fluids* **2019**, *4*, 101; doi:10.3390/fluids4020101

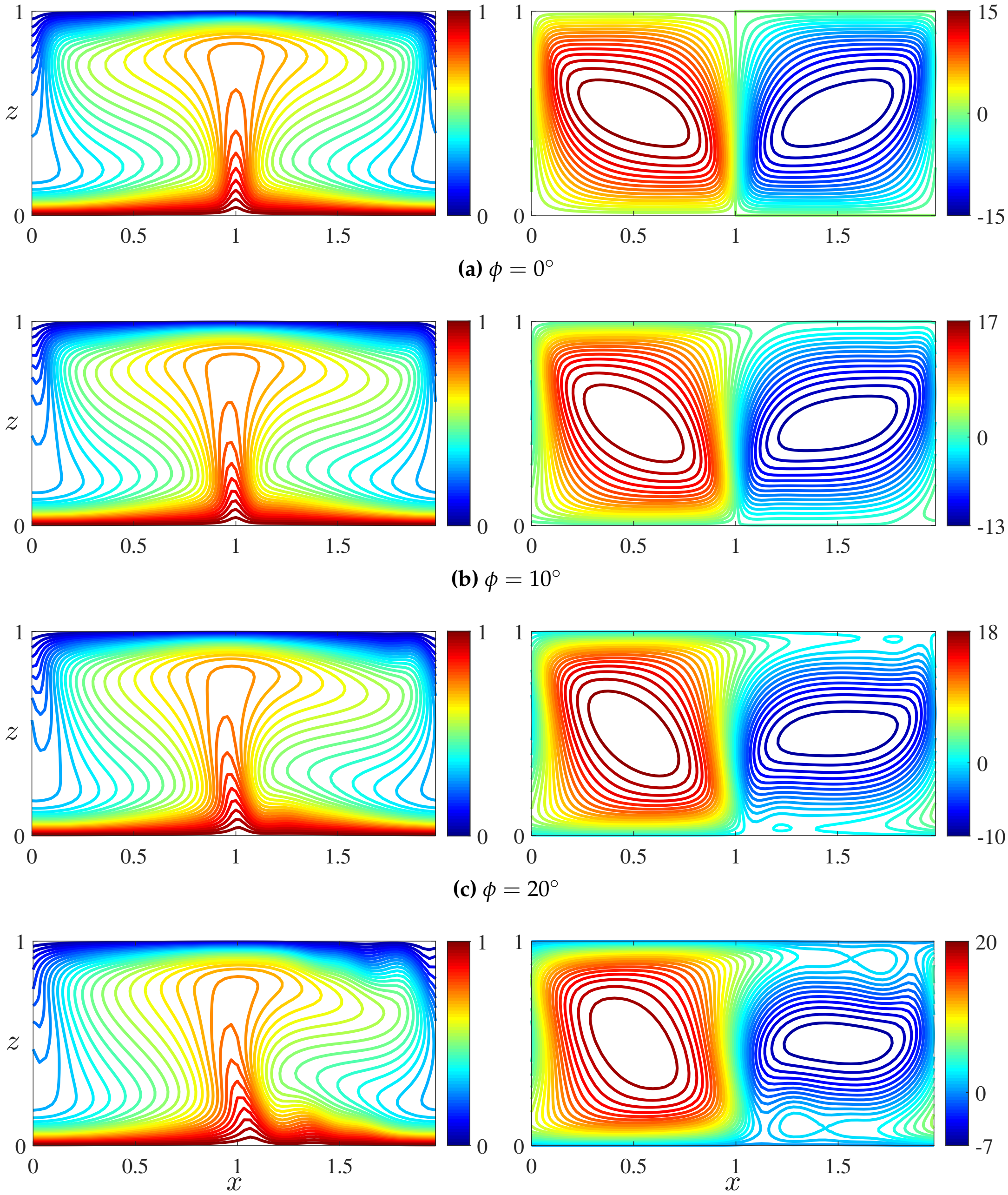

(a) $\phi = 0°$

(b) $\phi = 10°$

(c) $\phi = 20°$

(d) $\phi = 30°$

Figure 6. Isotherms (left) and streamlines (right) of steady convective states at $Ra = 500$ and $L = 2$. As the inclination angle is increased, the natural roll (positive ψ) becomes more vigorous (see the colorbar limits) and more tightly attached to the walls, while the antinatural roll (negative ψ) is suppressed and becomes detached from the walls. At $\phi = 30°$, the antinatural roll makes contact with the upper and lower walls only at certain localized points.

Chebyshev collocation method and the resulting algebraic eigenvalue problem is solved using Arnoldi iteration to obtain the leading eigenvalues and eigenfunctions.

Our results reveal that, at moderate Ra, the maximum convective growth rate $\sigma_m \equiv \mathrm{Re}\{\lambda_m\}/Ra$ for both the horizontal and inclined cases is independent of β, and the corresponding fastest-growing eigenfunction shares a similar spatial structure for different β. Hence, below we only present the results of our stability analysis at $\beta = 0$. Figure 8 shows the variation of σ_m as a function of ϕ at the aspect ratio $L_s = 2\pi/k_s = 2$. The inclination of the layer enhances the instability of the steady state,

Preprints (www.preprints.org) | NOT PEER-REVIEWED | Posted: 30 April 2019 doi:10.20944/preprints201904.0328.v1

Peer-reviewed version available at Fluids 2019, 4, 101; doi:10.3390/fluids4020101

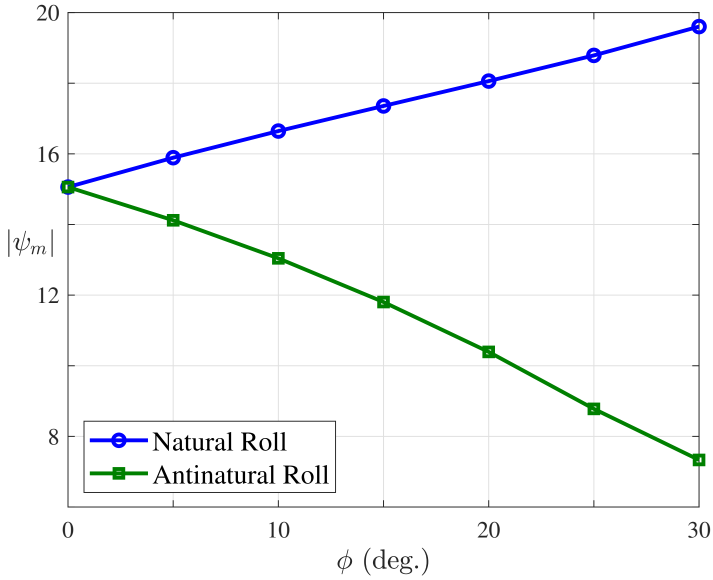

Figure 7. Magnitude of ψ_m for steady convective states as a function of ϕ at $Ra = 500$ and $L = 2$. ψ_m denotes the extremum ψ value corresponding to the natural roll with max(ψ) (positive) and antinatural roll with min(ψ) (negative). As ϕ is increased, the natural-roll motion is intensified, while the antinatural-roll motion is suppressed.

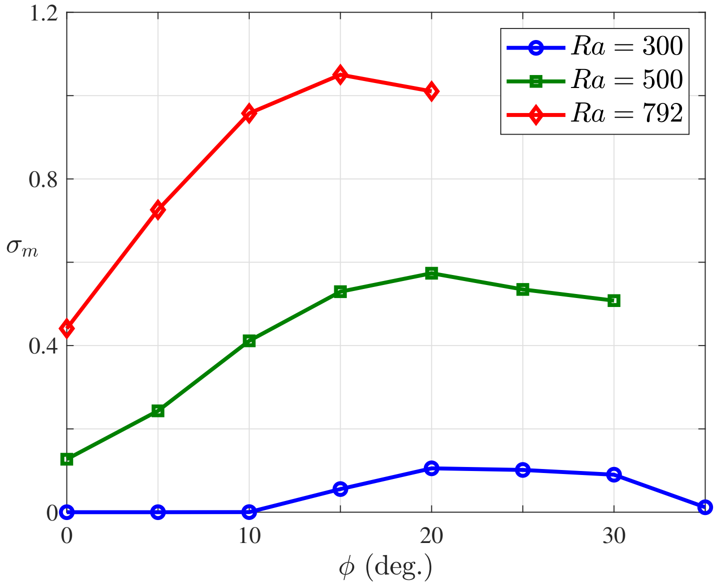

Figure 8. Variation of the maximum growth rate, σ_m, with ϕ at moderate Ra, $L_s = 2$ and $\beta = 0$. At $Ra = 300$, the steady state is marginally stable for $\phi < 10°$ and becomes weakly unstable at $\phi = 10°$. The same branch of steady states is not obtained at large ϕ for $Ra = 500$ and 792 using the present numerical scheme.

and for each Ra, there exists a peak in σ_m at particular angle ϕ_m. [Note that in our time-dependent DNS the increasing instability with ϕ generally causes the two-cell convection pattern to split into a four-cell pattern before ϕ_m is reached (table 1 and figure 8).] Moreover, the structure of the most unstable eigenfunction in figure 9 and the results in figure 10 confirm that the antinatural rolls are more unstable than are the natural rolls at moderate Rayleigh number, as also indicated by the DNS in § 3.1. Actually, as ϕ is increased, the natural roll of the steady state strengthens and becomes more tightly attached to the walls, and thereby is stabilized; on the contrary, the antinatural roll is suppressed and

Preprints (www.preprints.org) | NOT PEER-REVIEWED | Posted: 30 April 2019 doi:10.20944/preprints201904.0328.v1

Peer-reviewed version available at Fluids 2019, 4, 101; doi:10.3390/fluids4020101

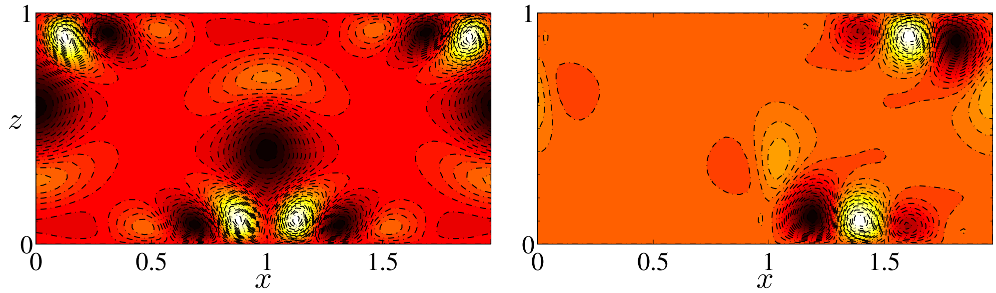

(a) $\phi = 0°$ **(b)** $\phi = 20°$

Figure 9. The fastest-growing 2D temperature eigenfunctions at $Ra = 500$, $L_s = 2$ and $\beta = 0$. For the horizontal case, reflection symmetry is satisfied and both of the natural and antinatural rolls are equally unstable. However, as ϕ is increased, the natural roll is stabilized and the instability of the antinatural roll is intensified.

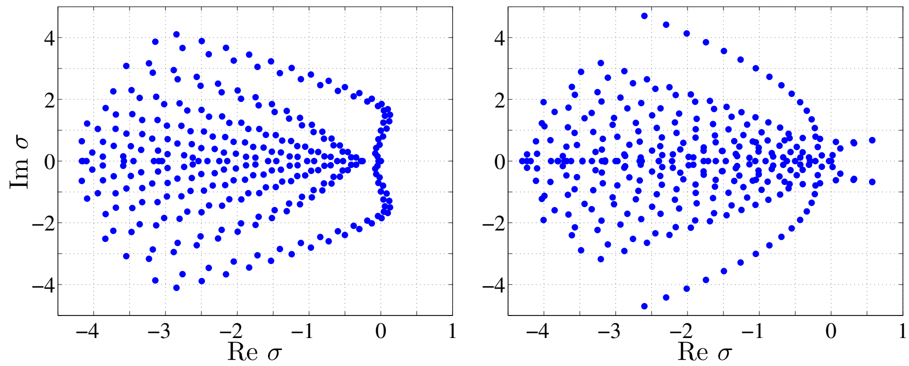

(a) $\phi = 0°$ **(b)** $\phi = 20°$

Figure 10. The leading eigenvalues, $\sigma = \lambda/Ra$, at $Ra = 500$, $L_s = 2$ and $\beta = 0$. All of the unstable modes for both the horizontal and inclined cases exhibit a similar structure as that of the corresponding fastest-growing mode in figure 9.

becomes detached from the walls, and thereby is destabilized. Thus, the increase of the maximum growth rate σ_m with ϕ in figure 8 is attributable to the destabilization of the antinatural roll.

4. Conclusion

In this study, we investigate the flow structure and dynamics of moderate-Ra convection in an inclined 2D porous layer uniformly heated from below. Using pseudospectral DNS, we show the evolution of the $O(1)$ aspect-ratio large-scale cellular flows as functions of Ra and ϕ. Our numerical simulation results indicate that the inclination of the layer breaks the reflection symmetry of the convective rolls in the wall-parallel direction. As the inclination angle ϕ is increased, the background shear flow strengthens, thereby intensifying the natural-roll motions and suppressing the antinatural-roll motions. Therefore, for increasing Rayleigh number Ra and at sufficiently large ϕ, the boundary layers of the antinatural roll become unstable prior to those of the natural roll. Interestingly, our DNS reveal for the first time the existence of spatially-localized convective states in single-species porous medium convection at large ϕ, which may be anticipated based on the gap in parameter values for linear and nonlinear stability of the basic shear flow [35].

To better understand the physics of inclined porous medium convection at different ϕ, the structure and stability of steady nonlinear convective states have also been investigated here at moderate Ra. We compute the steady solutions using a Newton–GMRES algorithm and then perform secondary stability analysis using Floquet theory. Consistent with the unsteady flow observed in our

DNS, the steady states appear in the form of large-scale convective rolls: one natural roll rotating in a counterclockwise direction; and one antinatural roll rotating in a clockwise direction. As the inclination angle is increased, the strengthening background mean flow enhances the motion of the natural roll causing it to more tightly attach to the upper and lower walls, but weakens the motion of the antinatural roll driving detachment from the walls, at least for sufficiently large ϕ. Moreover, Floquet analysis of these steady states reveals that before the antinatural roll is completely detached from the walls, the inclination of the layer stabilizes the boundary layers of the natural roll, but intensifies the boundary-layer instability of the antinatural roll. These analyses shed light on the development of moderate-*Ra* large-scale cellular flows at different inclination angles.

Author Contributions: Conceptualization, B.W. and G.P.C.; methodology, B.W. and G.P.C.; software, B.W.; validation, B.W.; formal analysis, B.W. and G.P.C.; investigation, B.W. and G.P.C.; resources, G.P.C.; data curation, B.W.; writing–original draft preparation, B.W. and G.P.C.; writing–review and editing, B.W. and G.P.C.; visualization, B.W.; supervision, G.P.C.; project administration, G.P.C.; funding acquisition, G.P.C.

Funding: This work was funded by NSF Award DMS-0928098 (G.P.C.).

Conflicts of Interest: The authors declare no conflict of interest.

1. Horton, C.W.; Rogers, F.T. Convection currents in a porous medium. *J. Appl. Phys.* **1945**, *16*, 367–370.
2. Lapwood, E.R. Convection of a fluid in a porous medium. *Proc. Camb. Phil. Soc.* **1948**, *44*, 508–521.
3. Graham, M.D.; Steen, P.H. Strongly interacting traveling waves and quasiperiodic dynamics in porous medium convection. *Physica D* **1992**, *54*, 331–350.
4. Otero, J.; Dontcheva, L.A.; Johnston, H.; Worthing, R.A.; Kurganov, A.; Petrova, G.; Doering, C.R. High-Rayleigh-number convection in a fluid-saturated porous layer. *J. Fluid Mech.* **2004**, *500*, 263–281.
5. Hewitt, D.R.; Neufeld, J.A.; Lister, J.R. Ultimate regime of high Rayleigh number convection in a porous medium. *Physical Review Letters* **2012**, *108*, 224503.
6. Wen, B.; Corson, L.T.; Chini, G.P. Structure and stability of steady porous medium convection at large Rayleigh number. *J. Fluid Mech.* **2015**, *772*, 197–224.
7. Liang, Y.; Wen, B.; Hesse, M.; DiCarlo, D. Effect of dispersion on solutal convection in porous media. *Geophys. Res. Lett.* **2018**, *45*, 9690–9698. doi:https://doi.org/10.1029/2018GL079849.
8. Metz, B.; Davidson, O.; de Coninck, H.; Loos, M.; Meyer, L. *IPCC Special Report on Carbon Dioxide Capture and Storage*; Cambridge University Press: New York, 2005.
9. Riaz, A.; Hesse, M.; Tchelepi, H.A.; Jr, F.M.O. Onset of convection in a gravitationally unstable diffusive boundary layer in porous media. *J. Fluid Mech.* **2006**, *548*, 87–111.
10. Nield, D.A.; Bejan, A. *Convection in Porous Media*, 4th ed.; Springer: New York, 2013.
11. Phillips, O.M. *Geological Fluid Dynamics: Sub-surface Flow and Reactions*; Cambridge University Press, 2009.
12. Schubert, G.; Straus, J.M. Transitions in time-dependent thermal convection in fluid-saturated porous media. *J. Fluid Mech.* **1982**, *121*, 301–313.
13. Kimura, S.; Schubert, G.; Straus, J.M. Route to chaos in porous-medium thermal convection. *J. Fluid Mech.* **1986**, *166*, 305–324.
14. Kimura, S.; Schubert, G.; Straus, J.M. Instabilities of steady, periodic, and quasi-periodic modes of convection in porous media. *J. Heat Transfer* **1987**, *109*, 350–355.
15. Aidun, C.K.; Steen, P.H. Transition to oscillatory convective heat transfer in a fluid-saturated porous medium. *J. Thermophys. H. T.* **1987**, *1*, 268–273.
16. Graham, M.D.; Steen, P.H. Plume formation and resonant bifurcations in porous-media convection. *J. Fluid Mech.* **1994**, *272*, 67–90.
17. MacMinn, C.W.; Juanes, R. Buoyant currents arrested by convective dissolution. *Geophysical Research Letters* **2013**, *40*, 2017–2022.
18. Tsai, P.A.; Riesing, K.; Stone, H.A. Density-driven convection enhanced by an inclined boundary: Implications for geological CO_2 storage. *Physical Review E* **2013**, *87*, 011003.
19. Sathaye, K.; Hesse, M.; Cassidy, M.; Stockli, D. Constraints on the magnitude and rate of CO_2 dissolution at Bravo Dome natural gas field. *PNAS* **2014**, *111*, 15332–15337. doi:10.1073/pnas.1406076111.

20. Akhbari, D.; Hesse, M.A. Causes of underpressure in natural CO_2 reservoirs and implications for geological storage. *Geology* **2017**, *45*, 47–50.
21. Bories, S.A.; Combarnous, M.A.; Jaffrenou, J. Observations des différentes formes d'écoulements thermoconvectifs dans une couche poreuse inclinée. *C. R. Acad. Sci. Paris A* **1972**, *275*, 857–860.
22. Bories, S.A.; Monferran, L. Condition de stabilité et échange thermique par convection naturelle dans une couche poreuse inclinée de grande extension. *C. R. Acad. Sci. Paris B* **1972**, *274*, 4–7.
23. Bories, S.A.; Combarnous, M.A. Natural convection in a sloping porous layer. *J. Fluid Mech.* **1973**, *57*, 63–79.
24. Caltagirone, J.P.; Cloupeau, M.; Combarnous, M. Convection naturelle fluctuante dans une couche poreuse horizontale. *C. R. Acad. Sci. Paris B* **1971**, *273*, 833–836.
25. Kaneko, T. *An Experimental Investigation of Natural Convection in Porous Media*; M.Sc. Thesis: University of Calgary, 1972.
26. Kaneko, T.; Mohtadi, M.F.; Aziz, K. An experimental study of natural convection in inclined porous media. *Int. J. Heat Mass Transfer* **1974**, *17*, 485–496.
27. Caltagirone, J.P.; Bories, S. Solutions and stability criteria of natural convective flow in an inclined porous layer. *J. Fluid Mech.* **1985**, *155*, 267–287.
28. Rees, D.; Bassom, A. The onset of Darcy–Bénard convection in an inclined layer heated from below. *Acta Mech.* **2000**, *144*, 103–118.
29. Rees, D.; Postelnicu, A. The onset of convection in an inclined anisotropic porous layer. *Int. J. Heat Mass Transfer* **2001**, *44*, 4127–4138.
30. Rees, D.; Storesletten, L.; Postelnicu, A. The onset of convection in an inclined anisotropic porous layer with oblique principle axes. *Transp. Porous Media* **2006**, *62*, 139–156.
31. Rees, D.; Barletta, A. Linear instability of the isoflux Darcy–Bénard problem in an inclined porous layer. *Transp. Porous Media* **2011**, *87*, 665–678.
32. Barletta, A.; Storesletten, L. Thermoconvective instabilities in an inclined porous channel heated from below. *Int. J. Heat Mass Transfer* **2011**, *54*, 2724–2733.
33. Barletta, A.; Rees, D. Local thermal non-equilibrium analysis of the thermoconvective instability in an inclined porous layer. *International Journal of Heat and Mass Transfer* **2015**, *83*, 327–336.
34. Celli, M.; Barletta, A. Onset of buoyancy driven convection in an inclined porous layer with an isobaric boundary. *International Journal of Heat and Mass Transfer* **2019**, *132*, 782–788.
35. Wen, B.; Chini, G.P. Inclined porous medium convection at large Rayleigh number. *J. Fluid Mech.* **2018**, *837*, 670–702. doi:10.1017/jfm.2017.863.
36. Walch, J.; Dulieu, B. Convection de Rayleigh–Béenard dans une cavité poreuse faiblement inclinée. *J. Phys. Lett.* **1982**, *43*, 103–107.
37. Moya, S.L.; Ramos, E.; Sen, M. Numerical study of natural convection in a tilted rectangular porous material. *Int. J. Heat Mass Transfer* **1987**, *30*, 741–756.
38. Sen, M.; Vasseur, P.; Robillard, L. Multiple steady states for unicellular natural convection in an inclined porous layer. *Int. J. Heat Mass Transfer* **1987**, *30*, 2097–2113.
39. Shi, Z.; Wen, B.; Hesse, M.; Tsotsis, T.; Jessen, K. Measurement and modeling of CO_2 mass transfer in brine at reservoir conditions. *Adv. Water Resour.* **2018**, *113*, 100–111. doi:https://doi.org/10.1016/j.advwatres.2017.11.002.
40. Wen, B.; Akhbari, D.; Zhang, L.; Hesse, M.A. Convective carbon dioxide dissolution in a closed porous medium at low pressure. *J. Fluid Mech.* **2018**, *854*, 56–87. doi:https://doi.org/10.1017/jfm.2018.622.
41. Wen, B.; Chang, K.W.; Hesse, M.A. Rayleigh-Darcy convection with hydrodynamic dispersion. *Physical Review Fluids* **2018**, *3*, 123801.
42. Boyd, J.P. *Chebyshev and Fourier Spectral Methods*, 2nd ed.; Dover: New York, 2000.
43. Nikitin, N. Third-order-accurate semi-implicit Runge–Kutta scheme for incompressible Navier–Stokes equations. *Int. J. Numer. Meth. Fluids* **2006**, *51*, 221–233.
44. Peyret, R. *Spectral Methods for Incompressible Viscous Flow*; Springer: New York, 2002.
45. Lo Jacono, D.; Bergeon, A.; Knobloch, E. Spatially localized binary fluid convection in a porous medium. *Physics of Fluids* **2010**, *22*, 909.
46. Lo Jacono, D.; Bergeon, A.; Knobloch, E. Three-dimensional spatially localized binary-fluid convection in a porous medium. *Journal of Fluid Mechanics* **2013**, *730*.